

Gravity Field over Northern Eurasia and Variations in the Strength of the Upper Mantle

Mikhail G. Kogan and Marcia K. McNutt

The correlation of long-wavelength gravity anomalies in northern Eurasia with seismic velocity anomalies in the upper mantle reverses in sign between western and eastern Eurasia. The difference between western and eastern Eurasia can be explained by the presence of a low-viscosity zone in the uppermost mantle beneath eastern Eurasia that is absent to the west. The location of the lateral change in viscosity corresponds with the geologic boundary between the older shields and platforms of the Baltics, Russia, and Siberia and the younger, geologically active mountain belts of eastern Asia. This relation provides evidence that differences in the strength of the upper mantle control the locus of intracontinental deformation.

The magnitude of the Earth's gravitational attraction varies by a few tenths of a percent over its surface. These fluctuations reflect how much the Earth's density structure departs from hydrostatic equilibrium and what mechanisms maintain such departures. For example, at long wavelengths the gravity field arises from the effects of mass anomalies in the mantle and the warping of density interfaces (such as the core-mantle boundary or the surface) in response to the flow driven by the buoyancy of these anomalous masses (1, 2). At shorter wavelengths, the gravity field is sensitive to the strength of the Earth's lithosphere supporting loads near or on the surface, such as topography (3, 4). On land, gravity data can be easily acquired from relatively inexpensive instruments and accurately measured to one part in 10^6 .

Until now, the only values of the gravity fields over northern Eurasia available to the public were those calculated from the spherical harmonic coefficients of the Earth's gravity field derived from tracking the perturbations of satellite orbits, sometimes supplemented with terrestrial gravity measurements where available. The resolution in the purely satellite solutions, such as GEM9 (5), is limited to spherical harmonic degrees $\ell \leq 15$ (wavelength ≥ 2500 km). Those solutions that incorporate land-based measurements, such as GEM10B (6), produce better resolution at higher degrees over some regions of the Earth at the expense of creating artificial artifacts over Eurasia and other regions that lack terrestrial control.

The Topographic Service of the Armed Forces of Russia made available digital gravity data at 10-km resolution and better than

0.5-mgal accuracy over the entire region encompassed by the former Soviet Union (Fig. 1B); these data increase by 20% the land area available for gravitational analysis at wavelengths less than 2500 km. Over 10 million point measurements collected between 1950 and 1985 were averaged within 5 arc min by 7.5 arc min cells to produce this data set.

Using helicopters and airplanes over 70% of the country, the Topographic Service sampled the gravity field every 1 to 4 km² according to very uniform and strict standards (7). The survey cost 2 billion rubles, more than 2 billion U.S. dollars at that time.

Addition of this new data to the satellite solutions should improve the accuracy at longer wavelengths as well. Comparison shows that the satellite solutions (5) currently predict correctly only 50% of the total gravity spectrum over northern Eurasia at wavelengths greater than 1000 km and only 75% at wavelengths greater than 3000 km. Solutions that incorporate terrestrial gravity data (6) show an even larger root-mean-square misfit to the new Russian data because of the risky practice of constraining the solution with predicted gravity anomalies in regions such as northern Eur-

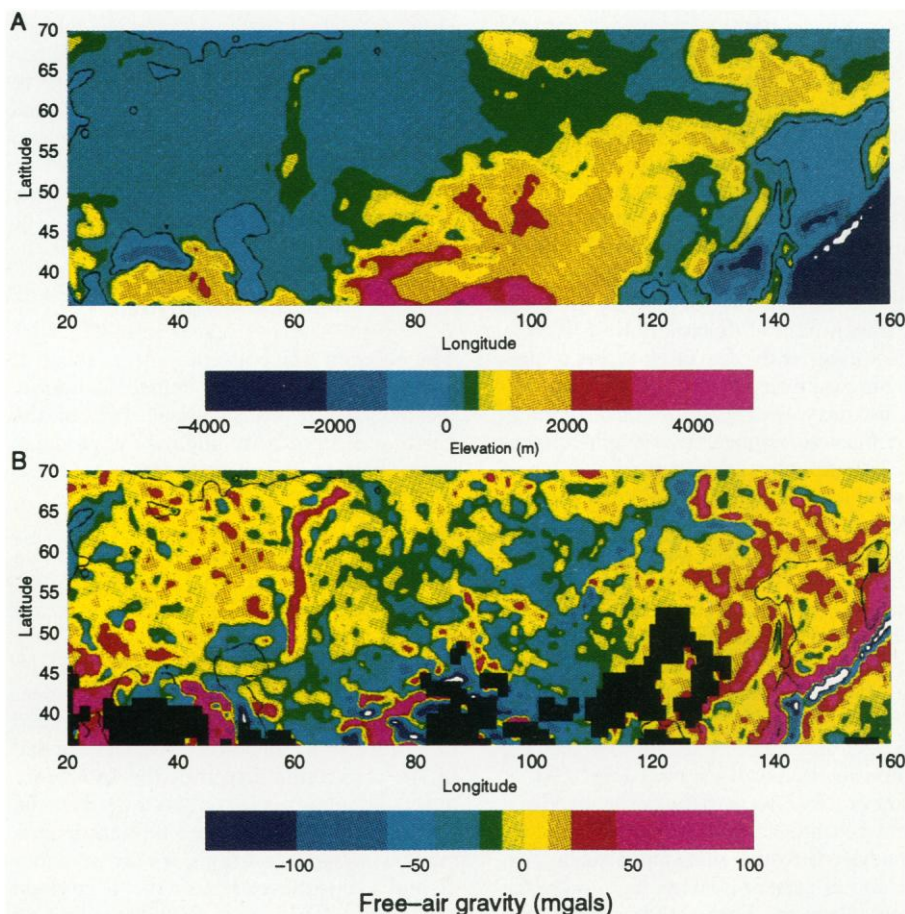


Fig. 1. Relief maps of (A) topography and (B) free-air anomaly over northern Eurasia. Sea-level contour is shown in black. Both data sets are 1° by 1° averages. Data courtesy of the Topographic Service of the Armed Forces of Russia.

M. G. Kogan is at the Institute of Mathematical Geophysics, Moscow, Russia, and M. K. McNutt is in the Department of Earth, Atmospheric, and Planetary Sciences, Massachusetts Institute of Technology, Cambridge, MA 02139.

asia that lack terrestrial control.

The availability of this new data, as well as a new solution for seismic velocity anomalies (8) beneath Eurasia, allows us to determine on a continental scale how strength variations in the upper mantle beneath the Eurasian plate might relate to the partitioning of the plate into geologically stable platforms in the north and west, and tectonically active areas in the south and east. The collision of the Indian subcontinent with the southern margin of Asia, which began 50 million years ago, has caused the uplift of the Himalayas and Tibet, as well as selective reactivation of older Paleozoic mountain belts, such as the Tien Shan and Altai Mountains, which are situated several thousands of

kilometers north of the collisional front (9). The zone of intense intracontinental deformation is unusually broad compared with what is observed on other continents at present and what is found in most examples from the geologic past; this raises the questions of what controls the width of the geologically active zone and how stress from the collision with India is transmitted laterally over such great distances. In this study, we investigate whether the mantle beneath the Eurasian plate has lateral variations in strength that determine the locus of intracontinental deformation.

Beginning with the original point data (10) sampled everywhere at better than 10-km resolution, we applied a simple running-mean filter to remove wavelengths shorter than 3000 km, the limit in the resolution of the seismic data that we used to model the gravity. Because we attempt only a regional analysis for mantle structure beneath Eurasia, we removed spherical harmonic degrees 1 through 6 from the data as well. These correspond to wavelengths equal to or greater than the radius of the Earth, and thus their modeling requires a whole Earth treatment (2, 11). The resulting band-passed gravity field is no longer associated with specific tectonic features on the Earth's surface (Fig. 2A). It displays gravity lows over the Baltic shield and central Siberia, flanked by a strong gravity high adjacent to the Kuril-Japan subduction zone and a gentler gravity high over the Russian platform. The mass heterogeneities that produce such broad-scale gravity anomalies are more likely to be maintained dynamically by flow in the mantle than to be

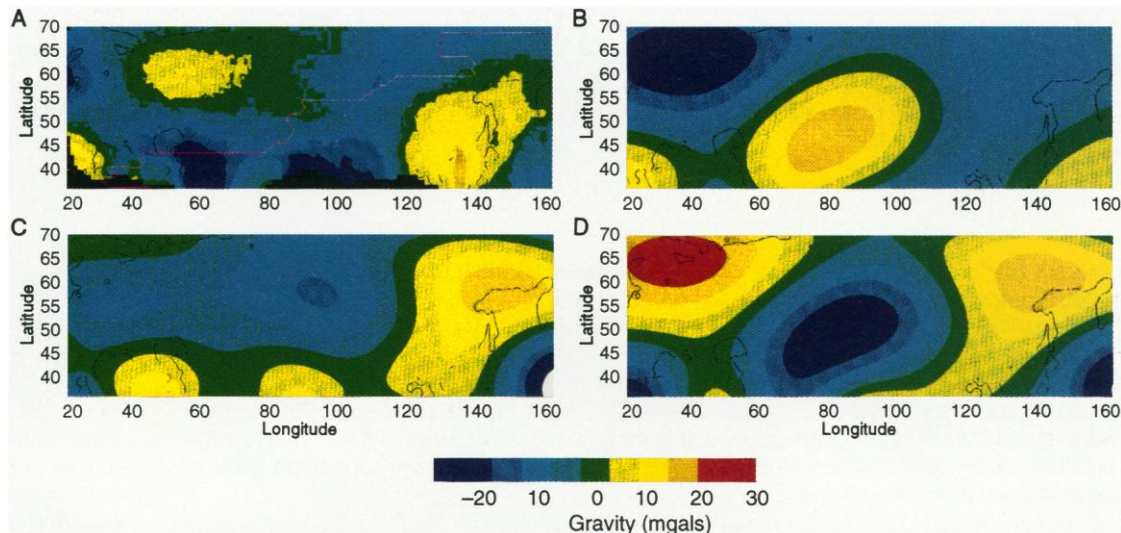


Fig. 2. Comparison of observed (A) and predicted long-wavelength gravity fields over northern Eurasia for spherical harmonic degrees 7 through 12. The predicted gravity anomalies are computed by convolving the seismic velocity anomalies of Su *et al.* (8) with kernels corresponding to the three mantle viscosity models—(B) MM1 ($\partial v/\partial \rho = 12$), (C) MM2 ($\partial v/\partial \rho = 3$), and (D) MM3 ($\partial v/\partial \rho = 12$)—in Fig. 3. Seismic anomalies in the uppermost 100 km were excluded from the calculation of predicted gravity on the assumption that anomalies within the lithosphere are isostatically compensated and thus have little gravity signal at these wavelengths. The red line running from the southwest to the northeast across (A) marks the approximate location of the geologic boundary between (i) stable platforms and shields to the west and (ii) newly forming or reactivated mountain belts to the east.

supported isostatically within the Eurasian lithosphere (12). Using the most recent model (8) of lateral variations in seismic velocity beneath Eurasia as a proxy for density heterogeneity in the mantle, we seek to assess to what extent the gravity field over Eurasia can be explained by these tomographically imaged seismic anomalies and to place constraints on the viscosity structure beneath the northern Eurasian lithosphere.

Relation Between Anomalous Mass and Gravity

The relation (2) between a thin sheet of anomalous mass $\delta\sigma_{\ell mi}$ of degree ℓ , order m located on the i th spherical shell of the Earth and the gravity anomaly it produces at the Earth's surface, $\delta g_{\ell mi}$, is

$$\delta g_{\ell mi} = \frac{4\pi\gamma(\ell-1)}{2\ell+1} G_{\ell i} \delta\sigma_{\ell mi} \quad (1)$$

where γ is Newton's gravitational constant and $G_{\ell i}$ is an array of dimensionless Love numbers. The Love numbers include the direct gravitational effect of the mass sheet as well as contributions to the gravity field from the warping of density interfaces caused by the convection driven by the anomalous mass. To obtain $G_{\ell i}$ one must solve the equations of continuity and motion given a set of boundary conditions, a viscosity model, and a constitutive relation between stress and strain. This array is independent of order m for an isotropic Earth. These Love numbers act as weighting functions to determine how mass anomalies of each harmonic

contribute at various depths to the predicted gravity field (Fig. 3).

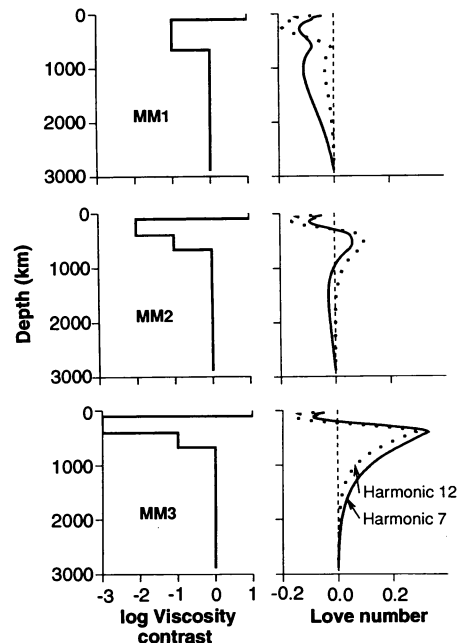


Fig. 3. Three viscosity models (left panel) and their corresponding Love numbers for spherical harmonic degrees 7 and 12 (right panel). The Love numbers are integrated with density variations of the given harmonic over depth to produce the predicted surface gravity field for that harmonic. For mantle model (MM) 1, positive mass anomalies (heavy material) at all depths produce negative free-air anomalies, whereas for MM2 and MM3, which have low viscosity zones in the uppermost mantle, heavy material between approximately 400 and 1000 km produces gravity highs.

Given a solution from seismic tomography for the seismic velocity anomaly $\delta v_{\ell mi}$ in the i th spherical shell lying between $r = r_1$ and $r = r_2$, the mass anomaly implied is simply

$$\delta \sigma_{\ell mi} = \frac{1}{\partial v / \partial \rho} \delta v_{\ell mi} (r_2 - r_1) \quad (2)$$

where $\partial v / \partial \rho$ relates the change in velocity to the change in density. The total gravity anomaly $\delta g_{\ell m}$ (or the geoid or topography, with suitable rescaling of the factor preceding the Love number) can be simply obtained by summing the terms in Eq. 1 over all spherical shells i . After the factors $\delta g_{\ell m}$ are calculated for all degrees and orders of interest, they can be used as the coefficients in an expansion of spherical harmonics to recover the gravity anomaly Δg in the spatial domain as a function of latitude θ and longitude ϕ .

A problem with the above formulation arises when, on account of source-receiver geometry, the seismic velocity anomalies $\Delta v(\theta, \phi, i)$ are not defined everywhere

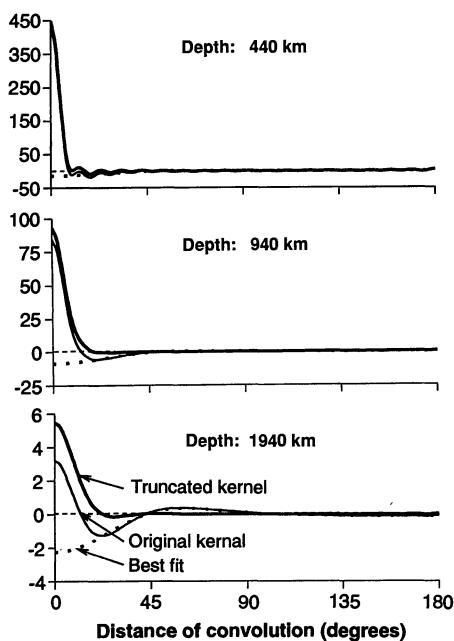


Fig. 4. Comparison of spatial kernels for dynamic isostasy with truncated kernels appropriate for a regional analysis for mass anomalies; at depths of 440, 940, and 1940 km. The thin solid curve shows the original kernel K_i obtained by summing up the Love numbers for the four-layer mantle viscosity model MM3 shown in Fig. 3. The dotted line shows the fit to the tail of the kernel at distances between 20° and 180° using Legendre polynomials up to degree 6. The thick solid curve is the truncated kernel K_i^t , which was used for convolution in the regional approach and has the desired properties of zero amplitude at distances beyond 20° while only differing from the original kernel at harmonics $\ell \leq 6$.

within the i th spherical shell. A spherical harmonic expansion with $\delta \sigma_{\ell mi}$ is not possible in this case, even though the anomalies may be well constrained beneath the region of immediate interest. In such a case, it is convenient to replace in Eq. 1 the multiplication in the wavenumber domain by a convolution, in the spatial domain, of the anomalous mass $\Delta \sigma$ with kernels $K_i(\cos \psi)$:

$$\Delta g(\theta, \phi, i) = \frac{2\gamma(\ell - 1)}{2\ell + 1} \iint \Delta \sigma(\theta', \phi', i) K_i(\cos \psi) \sin \theta' d\theta' d\phi' \quad (3)$$

$$K_i(\cos \psi) = \sum_{\ell} \frac{2\ell + 1}{2} G_{\ell} P_{\ell}(\cos \psi) \quad (4)$$

where ψ is angular distance between (θ, ϕ) and (θ', ϕ') and P_{ℓ} is the Legendre polynomial of degree ℓ . However, because the kernels K_i extend to the antipode of (θ, ϕ) , the integration in Eq. 3 extends over the entire Earth and is computationally intensive for an area the size of northern Eurasia. We know, however, that the net contribution of the integration in regions far removed from (θ, ϕ) is negligible if we consider only those higher harmonics for which a whole Earth treatment is unnecessary.

To take advantage of this, we truncated the kernels $K_i(\cos \psi)$ at values of ψ beyond some ψ_t such that the integration can be carried out only in the region of study and in an annulus extending ψ_t degrees around it. This truncation is accomplished in the null space of the convolution such that it has no effect on the frequencies of interest in the following manner. Suppose we have confined our regional analysis to harmonic degrees $\ell > \ell_{\max}$ because the longer wavelengths require a whole Earth treatment. Let us further require that the first ℓ_{\max} harmonics have been removed from $\delta \sigma_{\ell mi}$. Then an arbitrary combination of the first ℓ_{\max} Legendre polynomials may be subtracted from the expansion of K_i without having any effect on the convolution in Eq. 3. Our choice of the weighting function for the ℓ_{\max} Legendre polynomials that are subtracted from the expansion for K_i is such that it produces a function $K_i^t(\cos \psi)$ that matches as closely as possible K_i at $\psi > \psi_t$. We then define the truncated kernel $K_i^t(\cos \psi)$ as

$$K_i^t(\cos \psi) = K_i(\cos \psi) - K_i'(\cos \psi) \quad (5)$$

The truncated kernel has the property that it is zero, or nearly so, at $\psi > \psi_t$, and at all distances, it differs from the untruncated kernel only at degrees $\ell \leq \ell_{\max}$ (Fig. 4). When the convolution in Eq. 3 is accomplished using K_i^t rather than K_i , the result is computationally identical because $\Delta \sigma_i(\theta, \phi)$ has no power at the long wavelengths where

K_i^t differs from K_i . The operation is far more efficient in that the integration surface only extends ψ_t degrees beyond the immediate region of study. In practice, we found that for $\ell_{\max} = 6$, ψ_t can be as small as 20° without loss of accuracy (Fig. 5).

Seismic Velocity Beneath Eurasia

Several solutions for the seismic velocity structure beneath northern Eurasia were available for our analysis: the P-wave model of Hager and Clayton (2) and S-wave solutions from Zhang and Tanimoto (13) and Su *et al.* (8). The model of Zhang and Tanimoto covers only the upper 500 km of the mantle and displays an overall lower amplitude than the other two models at similar depths, but it agrees well in pattern with the model of Su *et al.* in the upper 400 km. The P-wave data of Hager and Clayton have poor resolution in the upper

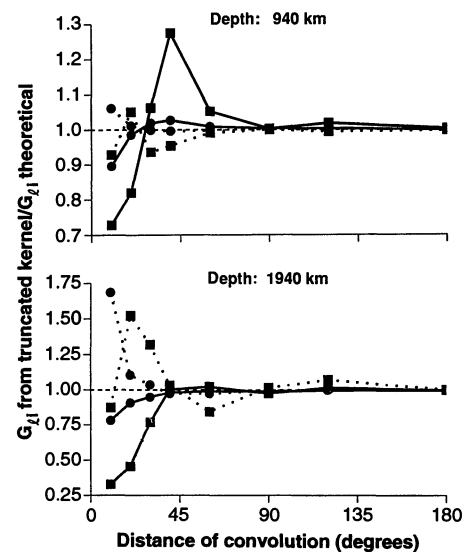
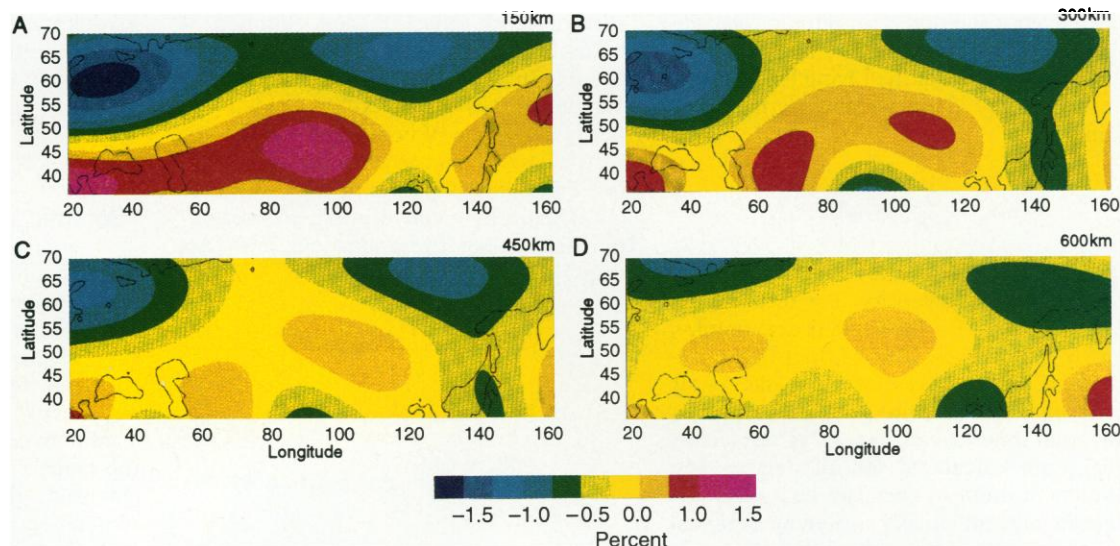


Fig. 5. Comparison of accuracy in the gravity anomaly computed as a function of distance over the Earth's surface to which the spatial convolution extends for monoharmonic ($\ell = 7$, solid lines; $\ell = 12$, dotted lines) mass anomalies at depths of 940 and 1940 km. A value of one indicates perfect agreement between convolution with the truncated kernels and with the original kernel. The solid squares show the result when the original kernel is simply set to zero beyond the convolution distance given on the horizontal axis. With that approach, it would be necessary to extend the convolution distance beyond 60° to obtain a gravity anomaly accurate to better than 10%. The solid circles show the result from our regional approach of truncating the kernel by subtracting from the original kernel a function that we found by fitting a Legendre polynomial with $\ell_{\max} = 6$ to the tail of the kernel. This improvement permits an accurate calculation of the gravity anomaly with convolution distances as short as 20° . We used MM3 for these calculations.

Fig. 6. Seismic velocity model of Su *et al.* (8) for spherical harmonic degrees 7 through 12 at various depths in the upper mantle. All panels represent the average over 100 km in depth [centered at (A) 150 km, (B) 300 km, (C) 450 km, and (D) 600 km] of the lateral velocity perturbation in each layer divided by the average velocity for the layer. The anomalies were then converted to percentages, and the signs were reversed; therefore, seismically fast regions appear blue (cold) and slow regions appear red (hot).



mantle (2), but agree well with the model of Su *et al.* in the lower mantle at degree and order 12 and less. Therefore, we consider the model of Su *et al.* to be the best currently available for this study because it covers the entire mantle, has good resolution in the upper mantle, and agrees well with other models in depth ranges where those models should be reliable.

The S-wave anomalies were provided (14) in terms of coefficients in a spherical harmonic expansion to degree and order 12 for $\delta v/v$, where δv is the velocity perturbation and v is the average layer velocity, in each of 143 spherical shells of thickness 20 km extending from the surface down to the core-mantle boundary. After removing the first six spherical harmonics, the data were converted to the space domain, averaged over shells 100 km thick, and sampled in blocks measuring 2° by 2° in each spherical shell beneath the Eurasian area of study (36° to 70° N, 20° to 160° E, and an area extending 20° around it).

In the upper mantle (Fig. 6), the seismic velocities show good correlation with known tectonic features. The high velocities that correspond to the old cratonic lithosphere beneath the Baltic Shield extend at least as deep as 300 km but fade below 450 km. There is some hint in the high velocities near 120° to 140° E of the descending Kuril slab. In the lower mantle, the anomalies are much lower in amplitude and no longer bear any relation to surface features. Near a depth of 2500 km, the amplitude increases slightly, reflecting increased heterogeneity near the core-mantle boundary.

Predicted Gravity

These seismic velocity anomalies presumably arise from departures of the Earth's density structure from a hydrostatic state

of stress and therefore are expected to drive convection in a viscous Earth. The amplitude and pattern of the predicted surface gravity caused by these anomalous masses, and the flow they induce, depend on (i) the viscosity stratification $\eta(z)$ that determines the shape of the kernel G_{ei} in Eq. 1 and (ii) the value of the conversion factor $\partial v/\partial \rho$ that relates seismic velocity to density in Eq. 2. We can use the observed gravity over northern Eurasia to constrain these quantities, which, in turn, depend on the temperature and mineralogy of the mantle.

We present results for three viscosity models that display similar viscosity contrasts for the lithosphere and lower mantle (15) but different structures for the upper mantle (Fig. 3). Mantle model 1 (MM1) had a uniform viscosity upper mantle ten times less viscous than the lower mantle. In MM2, the viscosity was reduced by one more order of magnitude between the depths of 100 and 400 km; and in MM3, the viscosity was decreased at these depths by yet one more order of magnitude (16). Thus, the models tested the sensitivity of the predicted gravity to the presence of a low-viscosity zone in the uppermost mantle. We only considered models of whole mantle convection and assumed free-slip at the surface and the core-mantle boundary.

We must assume a value for $\partial v/\partial \rho$ in Eq. 2 in order to convert the seismic velocity anomalies to density anomalies, which drive convection. This ratio may not be constant with depth because material properties that relate seismic velocity and density to temperature change with depth and because seismic velocity perturbations may be caused by changes in mineralogy, rather than temperature, in selected regions of the mantle (17). We experimented with depth-dependent mod-

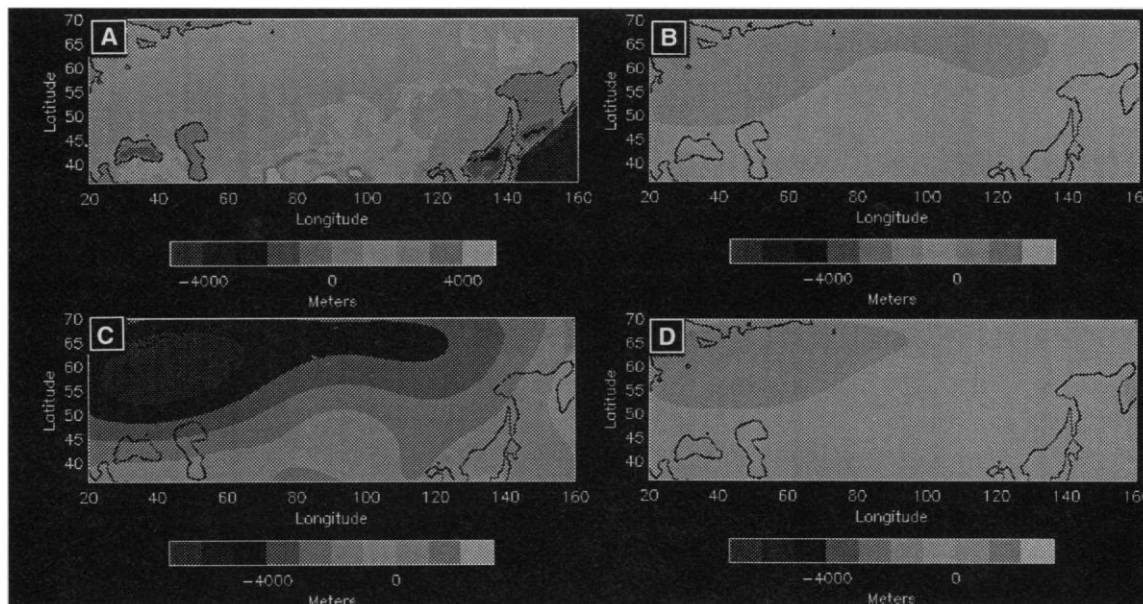
els of $\partial v/\partial \rho$ derived from a least-squares fit to the geoid at longer wavelengths (11); we found that, for the wavelengths of interest here, the predicted gravity is insensitive to the value of $\partial v/\partial \rho$ in the lower mantle and only depends on the average value for the upper mantle. Therefore, we assumed that $\partial v/\partial \rho$ was constant with depth as a first approximation and calculated, for each viscosity model, the value that produced a theoretical gravity field with the same peak-to-trough amplitude as the observed field.

Comparisons of the observed gravity at degrees and orders 7 through 12 with the gravity predicted by convolution of the density anomalies with truncated convolution kernels corresponding to the three viscosity models (Fig. 2) show that no single model produces a good fit across all of northern Eurasia. Rather, to the west of the line that marks the boundary between the geologically stable western region and the geologically active eastern region, the computed correlation between the observed gravity and that predicted by MM1 is positive; whereas to the east, it is negative and the coherence is low. For MM3, the opposite is true; the correlation is positive and the coherence is high for the eastern section only. The fit for MM2 is similar to that for MM3; but the coherence for the east is not as high, and $\partial v/\partial \rho$ must be reduced by a factor of 4 to get a reasonable amplitude for the gravity. The implication from these observations is that the viscosity model MM1 provides the best fit to the western region and MM3 better reproduces the pattern for the eastern region.

Dynamic Topography

In order to obtain an independent assessment of whether any of these three models

Fig. 7. Predicted warping of the Earth's surface at wavelengths greater than 3000 km. Obtained by convolving the seismic velocity model of Su *et al.* (8) with kernels corresponding to the three mantle viscosity models in Fig. 3: (A) observed, (B) MM1, (C) MM2, (D) MM3. The values of $\partial v / \partial p$ were chosen as in Fig. 2 to match the amplitude of the gravity field.



is reasonable, we computed the predicted surface deformation produced by dynamic flow beneath the plate. There is, unfortunately, no base level against which dynamic topography on the continents can be measured. For the ocean basins, where the thermal plate model provides just such a reference, dynamic topography does not exceed several hundred meters at the wavelengths with which we are concerned (18). Although the asthenospheric (uppermost mantle) viscosity beneath old continents might be higher, which allows for larger amplitude dynamic topography, 3 km is probably an upper bound on the long-wavelength variations in continental elevation that cannot be explained by isostatically compensated variations in crustal thickness. All three models produce an uplift of the Earth's surface east of the line separating the stable and active regions of the Eurasian continent (Fig. 7), as expected from the observed topography (19). However, on the basis of the amplitude of the dynamic topography, MM2 can clearly be rejected as it predicts uplift of eastern Asia by 6 km relative to the Baltic Shield. Given that the observed topography at long wavelengths is less than 2 km (Fig. 1A), the crust would actually have to be thinned beneath the mountain belts of central Asia for MM2 to produce a net (dynamic + isostatic) surface elevation that matched the observed. Models MM1 and MM3 predict more reasonable dynamic surface uplift of less than 1.5 km. Therefore, theoretical dynamic topography supports the inference from the gravity modeling that MM1 and MM3 are reasonable viscosity models for the mantle beneath western and eastern Eurasia, respectively.

Variations in Viscosity of the Eurasian Upper Mantle

Although we have not attempted an exhaustive search for models of mantle viscosity that are consistent with the new Russian gravity data, some generalizations concerning the viscosity models that are consistent can be made by an examination of the correlation between the observed gravity (Fig. 2) and seismic velocities (Fig. 6), keeping in mind the shape of the kernels in Fig. 3. Because the seismic velocity anomalies are larger in the upper mantle and the gravity kernels (for the wavelengths with which we are concerned) peak in the upper mantle, the net predicted gravity anomaly is largely controlled by the density structure in the upper 1000 km. Within this region, the Baltic Shield and the region surrounding Japan are fairly consistently underlain by fast material, except for the deepest layer beneath the Baltic and the shallowest layer beneath Japan. Therefore, it is difficult to explain why the Baltic would correspond to a gravity low and Japan a gravity high without invoking some lateral change in material properties, such as the existence of a low viscosity zone to the east. The relatively high viscosity in the uppermost mantle in the west couples to the Earth's surface the motion of the dense, high-velocity material beneath the Baltics, which causes a surface depression as the dense mass sinks. The net gravity effect is the sum of the mass deficit at the surface caused by the depression and the mass excess of the dense, sinking body; because of the attenuation of gravity with distance, the surface effect dominates, producing a gravity low. The effect of the

weak zone in the uppermost mantle beneath Japan is to partially decouple the dynamic effect of the sinking slab along the Pacific margin from the surface. A sinking body in or beneath a low-viscosity zone that has the same mass produces proportionally less surface deformation (20); therefore, the net gravity anomaly over a high-density body in the upper mantle can be positive (Fig. 3). Invoking a viscosity change in the upper mantle that coincides with the boundary between old and young continental crust in northern Eurasia thus explains why the long-wavelength gravity field (Fig. 2) is asymmetric about 90°E longitude, whereas the seismic velocity anomalies are symmetric about this line throughout the upper 1000 km (Fig. 6).

In our modeling, we have not taken into account the fact that the existence of a lateral variation in viscosity perturbs the flow field from that predicted by models with laterally uniform viscosity. When lateral variations in viscosity are included, the different spherical harmonic components relating mass anomalies to the flow are no longer independent and cannot be treated with exact analytical methods. Perturbation techniques can approximate the solution only if the lateral viscosity variation is one order of magnitude or less (21), and the computational problem is severe for the relatively short wavelengths considered in this study. Nevertheless, for our approach in which we perform spatial convolutions on more localized mass anomalies, we do not believe that the errors caused by a lack of explicit viscosity variation are severe. For example, it is possible to obtain a reliable estimate of the asthenospheric viscosity beneath the

western United States by computing, in the spatial domain, the rebound of the Earth's surface in response to the desiccation of the Pleistocene Lake Bonneville without considering the rebound of Fennoscandia in response to the melting of the glaciers, which yields a different and much higher viscosity. It would, however, be inappropriate to isolate the degree-two component in such an analysis without adopting a whole heterogeneous Earth treatment.

Within the limitations of our regional analysis, we consider the variation that we deduced in the viscosity to be fairly conservative and robust. For example, if we decrease the viscosity in the upper mantle beneath the eastern subregion (as in MM2) and simultaneously decrease $\partial v/\partial \rho$ to obtain the proper magnitude of the gravity anomaly, we produce an unacceptably large amount of dynamic topography. If we instead reduce the viscosity beneath the western subregion and invoke a negative value (22) for $\partial v/\partial \rho$ in order to produce the correct correlation between the velocity and gravity anomalies, the upper mantle viscosity beneath the old continental lithosphere of northwestern Eurasia departs substantially from that determined from modeling the response of the Fennoscandian lithosphere to removal of the Pleistocene glaciers (23). On the other hand, an additional modest increase in the viscosity of the upper mantle in the west or a decrease in the viscosity in the east is permitted by the data, with suitable rescaling of $\partial v/\partial \rho$, because the amount of dynamic topography is only constrained by an upper bound. Our choice of the shear-wave model of Su *et al.* (8) also was not critical. In a Cartesian analysis of gravity and P-wave velocities (2), Panasyuk and Kogan previously proposed a low viscosity zone of the same magnitude in the Siberian upper mantle (24).

Implications of Model for Eurasian Dynamics

Because viscosity is thought to depend strongly on temperature (25), the most obvious explanation for the variation in viscosity is that cooling of the upper mantle has penetrated to much greater depth beneath the much older [>1700 million years old (26)] western region as compared with the younger [250 to 800 million years old (26)] eastern region. Except for the interruption by the cold Kuril slab between 120° and 140°E , the eastern region is, on average, underlain by slower, and therefore presumably warmer, material in the upper 400 km of the mantle. If the average shear-wave velocity difference of nearly 1% between the west and east

sections is assumed to be entirely caused by temperature, the implied variations are of the order of 130°C , calculated with a value of $\partial v/\partial T = -0.35 \text{ m s}^{-1} \text{ }^\circ\text{C}^{-1}$ derived from laboratory calibrations (27). If we assume that viscosity drops exponentially as temperature increases, with an activation energy of approximately 500 kJ mol^{-1} , this sort of temperature increase would correspond to a viscosity ratio of 0.015 between the eastern and western sections, which is comparable to the observed ratio.

However, this interpretation of the velocity and viscosity variations in terms of temperature differences alone is surely flawed. The value we obtain for $\partial v/\partial \rho$, $12 \text{ km cm}^3 \text{ g}^{-1} \text{ s}^{-1}$, is significantly higher than the value of approximately $3 \text{ km cm}^3 \text{ g}^{-1} \text{ s}^{-1}$ obtained from Birch's law (28). Birch's law assumes that velocity and density are both varying with temperature and provides a fairly good match to the velocity-density relation one gets by fitting the low degrees and orders of the geoid to seismic velocity measurements in the lower mantle (2). Large apparent values of $\partial v/\partial \rho$ in the upper mantle have also been inferred from modeling of plate motions and a long-wavelength geoid on a global scale (11). One possible explanation for the high value for the effective $\partial v/\partial \rho$ beneath western Eurasia is that the temperature variations are, in part, chemically compensated by the development of a layer depleted in the major basaltic constituents (22). This would cause, for example, a high velocity, cold mantle root to have less negative buoyancy than predicted by thermal considerations alone, which is attributable to its lighter mineralogical composition. For the geologically younger, and presumably undepleted, regions to the east, the low effective value for $\partial v/\partial \rho$ in the upper mantle may indicate the presence of small degrees of partial melt or the development of dislocations in the solid state in response to the tectonic stress (29).

The lower viscosity that we derive for eastern Eurasia corresponds to an increased strain rate two orders of magnitude greater than in the west, assuming a Newtonian relation between stress and strain rate. If the collision of India with Asia has involved deformation of parts of the upper mantle between 100 and 400 km in depth, this variation in strain rate could explain, without requiring any differences in the properties of the continental crust or shallow-mantle lithosphere, why the collision of continental blocks (such as Italy, Arabia, and India) with the southern border of Eurasia created only narrow mountain belts in the west but broad zones of intracontinental deformation in the east (9).

Our conclusions from dynamic modeling of gravity and seismic velocity anomalies from northern Eurasia point to a revised view of continental tectonics—the physical properties of the upper mantle to depths as great as 400 km are affected by the thermal structure and stress history of the overlying continents, and lateral variations in these physical properties, in turn, dictate patterns of intracontinental deformation (30).

REFERENCES AND NOTES

1. M. A. Richards and B. H. Hager, *J. Geophys. Res.* **89**, 5987 (1984).
2. B. H. Hager and R. W. Clayton, in *Mantle Convection*, W. R. Peltier, Ed. (Gordon and Breach, New York, 1989), pp. 657–763.
3. D. W. Forsyth, *J. Geophys. Res.* **90**, 1223 (1985).
4. M. G. Kogan and M. K. McNutt, in *Composition, Structure, and Dynamics of the Lithosphere-Asthenosphere System*, K. Fuchs and C. Froidevaux, Eds. (Geodynamics Series 16, American Geophysical Union, Washington, DC, 1987), pp. 301–307; M. K. McNutt and M. G. Kogan, in *ibid.*, pp. 309–327.
5. F. J. Lerch, S. M. Klosko, R. E. Laubscher, C. A. Wagner, *J. Geophys. Res.* **84**, 3897 (1979).
6. F. J. Lerch, B. H. Putney, C. A. Wagner, S. M. Klosko, *Mar. Geod.* **5**, 145 (1981).
7. Special gravity teams from the Ministry of Geology used Soviet-built Worden-type gravimeters for this survey and, by making two visits to each new point to check for instrument drift, tied each station to a first-order network. The absolute gravity values for the first-order network were obtained with a free-fall gravimeter, which was calibrated to within $1 \mu\text{gal}$ of instruments used in France, the United States, Italy, and Japan. The point values were corrected for terrain within a radius of 200 km. The average value of each 10-km grid cell was corrected for the deviation of the average elevation of the gravity stations from the average elevation of the grid cell, as derived from topographic maps, with the use of the slope of the linear regression of free-air gravity versus elevation over small areas.
8. W.-J. Su, R. L. Woodward, A. M. Dziewonski, *Eos* **73**, 201 (1992).
9. P. Tapponnier and P. Molnar, *J. Geophys. Res.* **84**, 3425 (1979); B. C. Burchfiel and L. H. Royden, *Ecolgae Geol. Helv.* **84**, 599 (1991).
10. Although it is customary in studies of long-wavelength features to deal with a geoid that emphasizes the lower degree harmonics, we analyzed gravity directly because that is the quantity measured with the land gravimeters.
11. A. M. Forte, A. M. Dziewonski, R. L. Woodward, in *Dynamics of the Earth's Deep Interior and Earth Rotation*, J.-L. LeMouél, Ed. (American Geophysical Union, Washington, DC, in press).
12. For example, a near-surface mass of $3 \times 10^6 \text{ kg m}^{-2}$ is required to produce the 10-mgal high at 3000-km wavelength over the Russian platform at 60°N , 50°E if this load is supported by the lithosphere with an effective elastic thickness of 100 km or less. This mass anomaly would be equivalent to 1.5 km of surface relief, which is not seen (Fig. 1A), or a 5-km-thick, near-surface mass anomaly with the density of mantle rocks, which cannot be completely ruled out.
13. Y.-S. Zhang and T. Tanimoto, *Phys. Earth Planet. Inter.* **66**, 160 (1991).
14. W.-J. Su, thesis, Harvard University (1993).
15. Based on numerical experiments, we concluded that our results are sensitive only to the average viscosity in the lower mantle. For global modeling at longer wavelengths, the predicted gravity de-

- pend on the assumed viscosity at the core-mantle boundary.
16. Because there is no time dependence in this modeling, only ratios of the vertical viscosity structure enter into the formulation; the absolute magnitude of the reference viscosity (here taken to be the lower mantle) is not determined.
 17. A. M. Dziewonski and D. L. Anderson, *Phys. Earth Planet. Inter.* **25**, 297 (1981); S. P. Grand and D. V. Helmberger, *Geophys. J. R. Astron. Soc.* **76**, 399 (1984).
 18. M. K. McNutt and A. V. Judge, *Science* **248**, 969 (1990).
 19. For the calculation of dynamic topography, harmonics 1 to 6 were included so that the result could be directly compared with the observed topography.
 20. In this case, the sinking body would be compensated from below by deformation of the core-mantle boundary rather than from above by deformation of the Earth's surface. Again, at these wavelengths the gravity effect of the shallow source dominates; the gravity excess of the sinking body is larger in amplitude than the gravity low from deformation of the core-mantle boundary.
 21. M. A. Richards and B. H. Hager, *J. Geophys. Res.* **94**, 10299 (1989).
 22. A negative value for $\partial v/\partial \rho$ is possible if the density and seismic velocity anomalies are caused by variations in mantle chemistry rather than temperature. See T. H. Jordan, *Rev. Geophys.* **13**, 1 (1975).
 23. W. R. Peltier, R. A. Drummond, A. M. Tushingham, *Geophys. J. R. Astron. Soc.* **87**, 79 (1986).
 24. S. V. Panasyuk and M. G. Kogan, unpublished preprint.
 25. D. L. Kohlstedt and C. Goetze, *J. Geophys. Res.* **79**, 2045 (1974).
 26. J. G. Sclater, B. Parsons, C. Jaupart, *ibid.* **86**, 11535 (1981).
 27. M. Kumozawa and O. L. Angerson, *ibid.* **74**, 5961 (1969).
 28. F. Birch, in *The Earth's Crust and Upper Mantle*, P. J. Hart, Ed. (American Geophysical Union, Washington, DC, 1969), pp. 18-36.
 29. J. B. Minster and D. L. Anderson, *J. Geophys. Res.* **85**, 6347 (1980).
 30. We thank the Topographic Service of the Armed Forces of Russia for providing us with the gravity field, R. Clayton and T. Tanimoto for providing electronic versions of their seismic anomalies, and A. Lerner-Lam, B. Hager, T. Jordan, A. Forte, and S. Panasyuk for discussions. W. Su, R. Woodward, and A. Dziewonski permitted use of their S-wave model in advance of publication. M.G.K. is grateful for the use of the computer facilities at the Lamont-Doherty Geological Observatory while in residence as a visiting scientist. M.K.M. acknowledges generous support from the National Aeronautics and Space Administration.

Beyond Nature's Chiral Pool: Enantioselective Catalysis in Industry

William A. Nugent, T. V. RajanBabu, Mark J. Burk

Enantioselective catalysts produce organic compounds in enantiomerically enriched form. They are highly efficient tools for the synthesis of biologically active materials, such as pharmaceuticals and crop-protection chemicals, in which enantiomeric purity can be critical. The design of chiral ligands is the key to developing new enantioselective catalysts. Three unusual families of ligands have been used to develop practical technology for enantioselective hydrocyanation of olefins, ring-opening of epoxides, and hydrogenation of various compounds.

Enantioselective catalysis is bringing about a revolution in asymmetric synthesis. Seldom has there been an area of chemistry where the scientific goals are so challenging, the economic benefits so obvious, and the ethical reasons for doing the research so compelling.

Living organisms are masters of enantioselective catalysis. In general, when a living cell manufactures a chiral organic molecule, it selectively produces only one of the two nonsuperimposable mirror-image forms (enantiomers). To do otherwise is at best inefficient and at worst fatal. Biocatalysts (enzymes and ribozymes) promote the chemistry of life with exquisite efficiency and selectivity, but synthetic chemists have been slow to learn from nature's model.

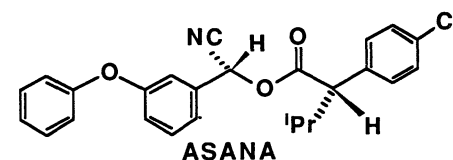
The authors are in Central Research and Development, Du Pont Company, Post Office Box 80328, Wilmington, DE 19880-0328.

Until recently, it was common practice for a pharmaceutical company to market a chiral drug as the racemate (1). This approach in effect meant that each dose of a drug was contaminated with an equal weight of an isomer, which usually had no therapeutic value but had the potential to cause unsuspected deleterious side effects. For example, the sedative thalidomide was marketed as a racemate. The desired sedative activity resides in the *R*-isomer, but the contaminant *S*-isomer is a teratogen, causing profound birth defects in babies born to mothers using the drug (2). The *R,R*-enantiomer of the tuberculostatic ethambutol can cause blindness. The lethal side effects associated with the pain-killer benoxaprofen (Oralflex) might have been avoided had the drug been sold as a pure enantiomer (3).

In the past, the selling of a racemic drug could be defended on the grounds that the

cost of manufacturing a single isomer could be prohibitive. Today, improvements in the technology for asymmetric synthesis, including the development of enantioselective catalysts based on metal complexes, make the development of new racemic drugs unacceptable. Asymmetric synthesis has advanced to the point where it should be possible to manufacture any drug as a single enantiomer.

The issue of enantiomeric purity is by no means limited to the field of pharmaceuticals. A case in point is ASANA (4) (i Pr = isopropyl), a synthetic pyrethroid insecticide which contains two asymmetric centers.



The potent insecticidal activity overwhelmingly resides in just one of the four possible stereoisomers. Moreover, the non-insecticidal stereoisomers exhibit significant cytotoxicity toward certain plant species. Thus ASANA, which is sold as a single stereoisomer, can be registered and used for crops whereas the mixed stereoisomers are not suitable. Add to this the need for chiral liquid crystals, enantiomerically pure polymers, and membrane components with applications in such diverse areas as drug delivery, separation technology, and optoelectronics. It is easy to understand the growing demand for efficient methods of producing enantiomerically pure compounds.

Conventional methods of asymmetric synthesis rely on the stoichiometric use of enantiomerically pure starting materials or reagents. In resolution by differential crystallization, for example, a racemic-product mixture is converted into a separable mixture of diastereomers with the use of a stoichiometric amount of an optically pure resolving agent. This method, however, requires recovery of the resolving agent and wastefully consumes precious starting materials and reagents to make the wrong enantiomer, which must then be racemized or discarded. Another conventional method is to build directly on products from nature's chiral pool. This approach is limited by the availability of inexpensive starting materials with the correct sense of chirality and with close structural similarity to the final target (5).

Perhaps the most important advantage of enantioselective catalysis, versus either of these stoichiometric procedures, is the feature of chiral multiplication. Under the right conditions, thousands of chiral product molecules can be produced by one molecule of catalyst. Chiral multiplication